Appl Phys A (2009) 96: 335–341
DOI 10.1007/s00339-009-5201-7

Applied Physics A
Materials Science & Processing

Femtosecond laser ablation of neurons in *C. elegans* for behavioral studies

Samuel H. Chung · Eric Mazur

Received: 24 October 2008 / Accepted: 3 March 2009 / Published online: 25 March 2009

Abstract Femtosecond laser ablation selectively dissects subcellular components of the *C. elegans* neuronal circuit with submicrometer precision for studying the neuronal origins of behavior. We describe the theoretical basis for the high precision of femtosecond laser ablation in the target bulk. Next, we present the experimental setup and a worm rotation technique to facilitate imaging and surgery. We describe the damage caused by different pulse energies on cell bodies and neuronal fibers. Finally, we discuss the regrowth of neuronal fibers after surgery and its impact on behavioral study.

PACS 42.62.Be · 87.19.L- · 87.64.Mn · 87.80.Fe

1 Introduction

The nematode worm *Caenorhabditis elegans* is an extremely useful model organism for studying the neuronal origins of behavior [1]. The worm nervous system is composed of merely 302 neurons, is mostly invariant among individuals, and completely specifies worm behavior [2]. Similar to reverse engineering of electrical circuits, elimination of specific neuronal cells or components yield behavioral deficits which illuminate the role of the lesioned structures in generating behavior. While powerful genetic techniques can perturb the neuronal circuit, the transparency and small diameter of *C. elegans* also permits laser ablation within the worm. For decades, researchers have ablated entire cell bodies with nanosecond and picosecond conventional lasers to identify the neuronal functions; however, the resolution of conventional laser ablation is insufficient to selectively dissect subcellular parts [3]. The submicrometer precision of femtosecond laser ablation in the bulk [4] opens the door to subcellular neuronal dissections and a subcellular understanding of the origins of behavior. In this paper, we first describe a simplified model behind the bulk precision of femtosecond laser ablation. Second, we present the experimental setup and a method to hold worms in a fixed position for imaging and surgery. Third, we state the pulse energy dependence of damage for cell body and neurite (i.e., neuronal fiber) ablation. Finally, we describe post-surgery axonal regrowth that may restore neuronal functions that contribute to behavior.

2 Theoretical background on surgical precision

While the physics of laser ablation is well understood [5, 6], femtosecond laser-induced breakdown remains an active research field [7]. Most of the early femtosecond laser ablation research studied the breakdown [8], damage, and micromachining [9] of simple transparent materials, such as glass [10, 11] and water [12]. These studies uncovered unique characteristics of femtosecond laser ablation, such as ablation thresholds, sub-diffraction-limited damage volumes, and localized damage in the material bulk. Ablation of transparent biological media is similar to ablation of in-

S.H. Chung (✉)
School of Engineering and Applied Sciences, Harvard University, 9 Oxford Street, Cambridge, MA 02138, USA
e-mail: samchung@post.harvard.edu

E. Mazur
Department of Physics and School of Engineering and Applied Sciences, Harvard University, 9 Oxford Street, Cambridge, MA 02138, USA
e-mail: mazur@physics.harvard.edu
Fax: +1-617-4959837

organic media because the same absorption processes are involved.

To perform surgery, the target material must absorb incident light energy. The manner in which absorption occurs partially determines the magnitude and spatial distribution of damage. Two primary absorption mechanisms involved in femtosecond laser ablation are nonlinear multiphoton absorption and avalanche ionization: typically, avalanche ionization absorbs most of the pulse energy but nonlinear absorption determines where that energy is absorbed [13]. In the remainder of this section we describe the intensity threshold for nonlinear absorption, its contribution to damage localization, and the effect of laser repetition rate on ablation precision.

Intensity threshold

In conventional laser ablation using lasers of ultraviolet (UV) to near-infrared wavelengths, a pulse of light impinging on a material can be absorbed if the photon energy is large enough to ionize valence electrons. Single photons of short wavelengths, such as those in the UV, can bridge the energy gap of transparent materials and be absorbed. Visible or near-infrared photons, which have longer wavelengths and do not bridge the energy gap, can still be absorbed when multiple photons are absorbed simultaneously (Fig. 1a). Absorption depends on the optical intensity,

$$I = \frac{E}{A\tau}, \tag{1}$$

where E is the pulse energy, A is the beam cross-sectional area, and τ is the pulse duration. The intensity is directly proportional to photon flux as well as the probability of finding a photon at a given place and time. Figure 1b shows the dependence of absorption, α, on intensity for the three absorption scenarios in Fig. 1a. If a single photon can bridge the energy gap, the amount of absorption depends only on the number of incident photons; thus, absorption is linearly related to intensity. If k photons are required to bridge the energy gap, k photons must be simultaneously present at the same location, an event with probability proportional to I^k. Thus, the absorption is proportional to I^k, a nonlinear dependence on intensity. The light from two-photon microscopes is absorbed under the $k = 2$ condition. At 800 nm, a typical wavelength for femtosecond lasers, 5 photons are required to ionize water, the primary component of biological media.

As the order of the absorption increases, the intensity dependence of the absorption approaches a threshold condition for nonlinear absorption, $I > I_{\text{th}}$ (Fig. 1c). The intensity threshold is a convenient approximation for determining the spatial extent of absorption. While some absorption occurs below the threshold, the tight focusing conditions normally employed for surgery produce a sudden, rapid increase in intensity near the focus minimizing the space where subthreshold absorption occurs.

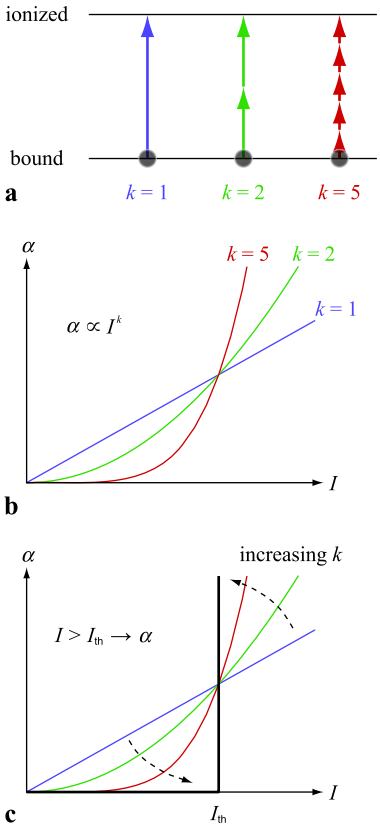

Fig. 1 Intensity dependence of the nonlinear absorption. (**a**) At different wavelengths, different numbers of photons are absorbed simultaneously to ionize electrons. (**b**) Absorption at a given wavelength is proportional to the kth power of the intensity, where k is the number of photons absorbed simultaneously. (**c**) The intensity dependence of the nonlinear absorption approaches a threshold condition as k increases

Localization of absorption and damage

Figure 2 shows a microscope objective focusing laser light toward the right. The solid lines demarcate the cross section of the beam, and the corresponding intensity for the beam profile is plotted below the diagram. Following from (1) the intensity peaks at the focus where the cross-sectional area is minimized. Many conventional laser ablation techniques rely on linear absorption, which is proportional to intensity. In those techniques, linear absorption and damage (red shading in Fig. 2a) occur throughout the beam path. In contrast, femtosecond laser ablation relies on nonlinear absorption, which depends on the intensity threshold. Only at the focus is the intensity sufficient to cause absorption. Thus, absorption and damage are localized to the focal volume (see shading in Fig. 2b). Note the lack of absorption to the right and left of the focal volume even though the laser beam passes

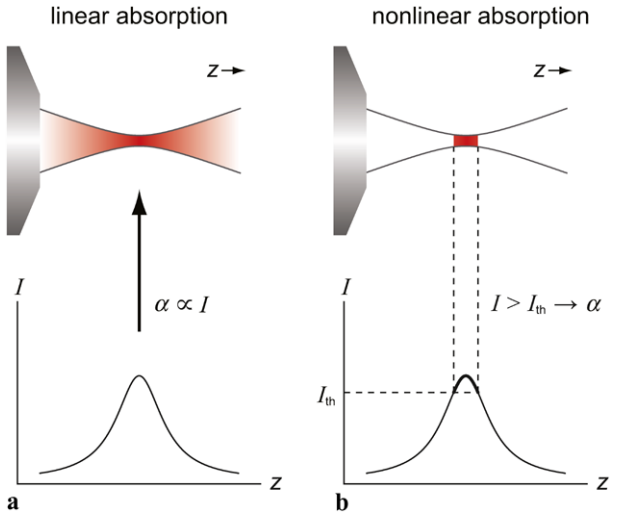

Fig. 2 Confinement of absorption and damage along the intensity profile of a focused laser beam due to intensity threshold. (**a**) Linear absorption is proportional to intensity and leads to absorption and damage (*red shading*) all throughout the beam path. (**b**) Nonlinear absorption depends on intensity threshold and leads to localization of absorption and damage

through that space. Even the surgeries that rely on subthreshold nonlinear absorption (see the following text) exhibit localized absorption at the intensity maximum because of the strongly nonlinear dependence of absorption.

The pulse energy must be minimized in order to limit damage to the space where optical absorption occurs. Excess energy spreads outward as heat and shock waves, which raise temperature, break chemical bonds, and disrupt tissue. As indicated by (1), the pulse energy can be minimized while maintaining $I = I_{\text{th}}$ by tight focusing (small A) and by making the pulse ultrashort (small τ). Femtosecond laser pulses of only 2–3 nJ focused with 1.4 numerical aperture (NA) objective already exceed the intensity threshold at the focus, but the damage caused by these pulses is limited to a submicrometer range [14].

There are three important practical points to note about femtosecond laser ablation in a sample. First, the sample's linear absorption at the laser wavelength must be zero (i.e., the sample must be transparent) as linear absorption typically dominates nonlinear absorption. Second, the target volume must be within the working distance of the microscope objective or lens focusing the laser pulses. Third, any optically accessible location in a transparent sample can be damaged because energy deposition no longer depends on linear absorption of the target at the laser wavelength.

Repetition rate

The preceding paragraphs described the damage caused by absorption of an individual pulse; however, the laser repetition rate also affects the magnitude and spatial distribution

Table 1 Laser ablation regimes

Laser type	Repetition rate	Absorption mechanism	Damage mechanism
Oscillator	10–100 MHz	Subthreshold	Cumulative
Amplified	1–100 kHz	Above threshold	Single-shot

of damage [15]. Ablation caused by femtosecond lasers can be divided into two regimes depending on the laser repetition rate: megahertz and kilohertz (Table 1). Femtosecond oscillators typically operate in the megahertz range while amplified systems typically operate in the kilohertz range. The boundary between the two regimes (around 1 MHz) is set by the time required for heat to diffuse out of the focal volume, about 1 μs for a 1 μm^3 volume [16]. At megahertz repetition rates successive pulses arrive faster than the deposited energy can diffuse out of the focal region leading to heat accumulation and further damage around the focus. In contrast, at kilohertz repetition rates the energy from each pulse diffuses out of the focal region before the next pulse arrives, so each single shot is a temporally isolated event. As such, damage remains confined to the focal volume regardless of the number of pulses.

The precise damage mechanisms for the two regimes are still being investigated. Previous papers established that damage in the megahertz range is thermally induced [5, 17]; however, recent theoretical work suggests that the cumulative temperature rise in the focal volume might be as low as 1–10°C [6]. If this calculation is confirmed experimentally, chemical effects, such as free-electron-induced bond breaking, could be the dominant damage mechanism in the megahertz regime [6]. Damage in the kilohertz range is created by small explosions of submicrosecond duration which are thermoelastically generated [6, 18].

The choice of laser repetition rate for surgery depends on the application. Surgeries in the megahertz range have higher spatial resolution due to the higher precision of the damage mechanism and lower subthreshold pulse energies. However, if the damage mechanism is thermal, collateral damage could extend beyond the focal volume and might be difficult to detect. Surgeries in the kilohertz range deliver less total energy to the sample due to the decreased repetition rate. While the spatial resolution is lower, damage is unlikely to extend beyond the focal volume because the laser pulse energy diffuses away between pulses and does not accumulate. Thus, megahertz-regime ablations (oscillators) might be desirable for processing nonliving biomaterials or fixed samples while kilohertz-regime ablations (amplified systems) might be better suited for surgeries on living samples, which are more sensitive to chemical damage and fluctuations in temperature.

3 Experimental setup

Figure 3a shows the femtosecond laser ablation setup [14] which consists of a femtosecond laser integrated into an epi-fluorescence microscope. Light from a mercury-arc lamp excites worm green fluorescent protein (GFP) whose fluorescence is captured by a CCD camera for imaging. A regeneratively-amplified titanium:sapphire laser system produces 100-fs pulses at 1–10 kHz for ablation. The 1.4-NA oil-immersion objective tightly focuses laser pulses into the worm, which is mounted on a positioning stage with nanometer resolution. To maintain optical alignment, all the optics remain fixed in position; we move the stage to position the worm for ablation.

Because the energy at the focus is experimentally more accessible than the intensity, we report energy thresholds rather than intensity thresholds. The two thresholds are related by (1).

During the early stages of larval development, imaging and ablation can occur anywhere in the worm; however, increasing turbidity and pigmentation limit the imaging depth in the body of the worm to about 50 μm by the young adult stage. Because the adult worm diameter is about 100 μm, much of the worm is beyond the imaging depth. Imaging and ablation is still possible on any target within adult worms by rotating worms so the target is closest to the coverslip. Unfortunately, when a coverslip is placed onto adult worms on a flat agarose pad the protruding vulva is pushed to the side consistently forcing worms into a lateral imaging orientation (see Fig. 3b, top).

We developed a method to hold worms in any flat-lying orientation [19]. We polymerize polydimethylsiloxane (PDMS) against the grooves of a 12-in long-playing (LP) vinyl record to create a negative replica mold (see Fig. 3c). Agarose fabricated against the ridges of the PDMS mold has channels which hold worms in a fixed orientation even when the coverslip is added (see Fig. 3b, bottom).

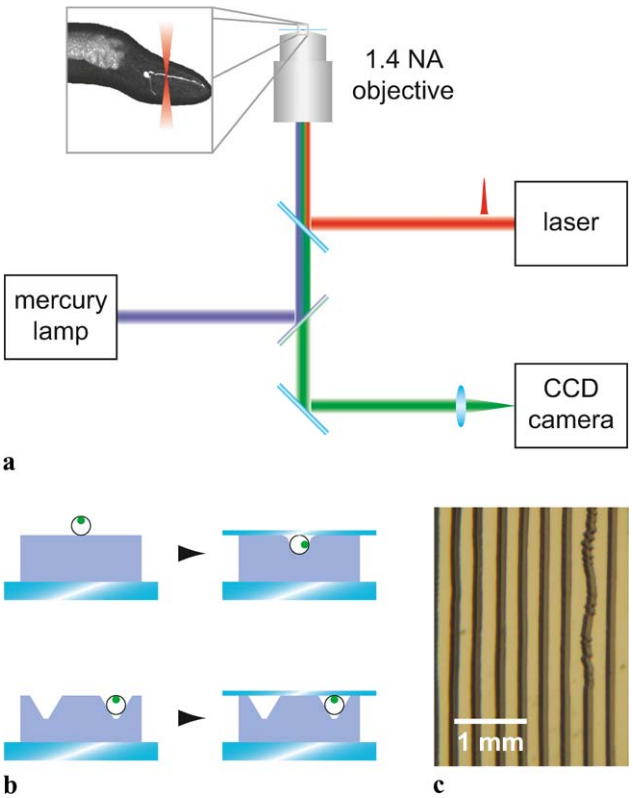

Fig. 3 (**a**) Epifluorescence microscope with integrated femtosecond laser for surgery. (**b**) Preparation of worms for imaging and surgery. *Top*: worms lying on flat agarose pad are pushed into lateral orientation by introduction of coverslip. Neuron (*green spot*) is far from coverslip, complicating imaging and surgery. *Bottom*: worms lying in channeled agarose maintain orientation when coverslip is added keeping neuron close to coverslip. (**c**) Bright-field image of vinyl record PDMS mold used to make channeled agarose

4 Pulse energy dependence of damage

The laser pulse energy strongly influences the precision of surgery. Pulses of low energy do not reach the intensity threshold or stimulate ablation while pulses of high energy produce collateral damage because too much ablation occurs. At 1.4-NA focusing and a pulse duration of 100 fs, the energy threshold for kilohertz-regime ablation of biological material is about 1 nJ [4, 20]. The exact energy threshold depends on the depth of the target (see Sect. 3), and the laser power output fluctuates slightly, so we typically fix our pulse energy well above the threshold at 2.5–3.0 nJ for all surgeries. With exposures of 0.1–0.2 s, pulses of these energies will consistently ablate biological structures if they can be imaged clearly and targeted. In *C. elegans* we use femtosecond laser ablation to ablate neuronal fibers (i.e., dendrites and axons) and cell bodies.

Severing neuronal fibers with femtosecond laser ablation eliminates specific neuronal connections along the fiber and their behavioral contribution but spares the rest of the neuron and its function. Figure 4 shows the dependence of neuronal fiber damage on pulse energy in the kilohertz repetition rate regime. Pulses with energies below the ablation threshold photobleach rather than ablate fibers leaving their function intact. Photobleached regions regain fluorescence within seconds as fluorophores diffuse through the intact, undamaged structures. Pulses with an energy in the range 0.5–1.5 nJ or misaimed pulses of higher energy result in "pearling", where the fluid within the fiber collects into regularly-spaced spheres. Although severed fibers can also pearl, a pearling state generally indicates an incomplete disruption of a fiber [21]; it is currently unknown if a pearled neuronal fiber is functional. Accurately-aimed pulses above the ablation threshold completely and cleanly sever neuronal fibers, eliminating their function.

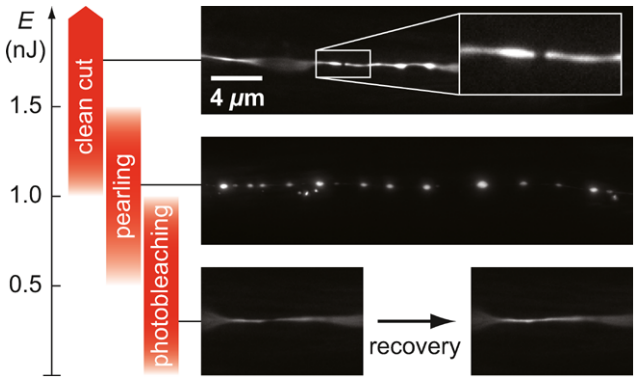

Fig. 4 Pulse-energy dependence of neuronal fiber damage at kilohertz repetition rate. *Top*: pulses with energies above the threshold (about 1 nJ) cleanly sever neuronal fibers. *Middle*: pulses with near-threshold energies cause "pearling". *Bottom*: pulses with subthreshold energies photobleach rather than ablate. Fiber fluorescence recovers in seconds. Energy scale is approximate. Scale bar applies to all images

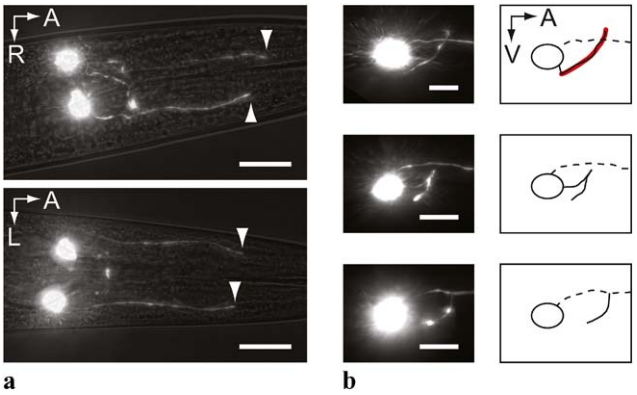

Fig. 5 Regeneration of amphid fibers. Surgery locations marked by arrowheads. Corner arrows show directions (ventral, right, left, anterior) in images. (**a**) Amphid dendrites do not regrow after surgery in L1 (*top*) or L4 (*bottom*). Images taken in adult stage. Maximum projection of GFP fluorescence z-stack overlaid with bright field image. Scale bars are 20 μm. (**b**) Amphid axons regrow after surgery in L1. Line drawings show dendrite (*dotted line*), axon (*solid line*), and nerve ring (*red*), which appears flat because it is viewed along edge. *Top*: normal axon in control worm runs ventrally to ring and then anterodorsally up ring. *Middle*: regrown axon extends from cell body to nerve ring, turns and then follows ring posteroventrally. Original axon cut near cell body and not visible. *Bottom*: regrown axon sprouts from dendrite and follows ring posteroventrally. Images taken 16 h after surgery. Maximum projection of GFP fluorescence z-stack. Scale bars are 10 μm

While femtosecond lasers permit the ablation of subcellular components (e.g., neurites) of neurons and the elimination of part of the neuronal function, they can also be used to ablate whole cell bodies and eliminate the entire neuronal function. Subcellular laser ablation often yields different behavior from whole cell ablation, and both provide insights into the functions of the targeted neuron [19]. Furthermore, as a control, we can compare worm behavior after femtosecond laser ablation of cell bodies to previously-published descriptions of worm behavior after conventional (i.e., ns or ps) laser ablation of cell bodies. We ablate cell bodies by irradiating several times for 0.5 s each time. Typically the plasma membrane remains intact after ablation confirming localization of damage, and the cell loses fluorescence and function over a time period of 24 h. Irradiating the cell body with 10-nJ pulses eliminates cell function within a few hours of surgery but increases the chance of collateral damage [22]. Pulse energies above 10 nJ lead to cell rupture and puncture of the cuticle if the cell is superficial.

5 Regrowth of neuronal fibers after surgery

One interesting recent discovery in *C. elegans* is the regrowth of neuronal fibers after transection by femtosecond laser ablation [23]. In principle, regrowth can restore neuronal functions previously eliminated by surgery. If the regrown fiber is functional, the post-surgery assay will not detect a behavioral deficit and therefore not identify the contribution of the fiber. Although many neuronal fibers regrow after transection, thus far, only one publication in *C. elegans* has presented evidence of functional regeneration [23]. In agreement with several publications on *C. elegans* regeneration [24–26], we find that neurites regrow to varying degrees depending on neuronal type, fiber type (i.e., dendrite or axon), age of the worm, and ablation location.

After hatching from the egg, worms develop through four larval stages (L1–L4) before molting to the adult stage. Imaging and behavioral assay confirm that amphid dendrites do not regenerate after severing during the L1, dauer, L4, or adult life stages [14, 22]. Figure 5a shows amphid dendrite cuts made in L1 (top) and L4 (bottom) persisting into the adult life stage. In contrast, amphid axons regenerate after severing in the L1, L2, and L4 [22], but not the adult stage [26]. The morphology of the regrown axon is significantly different from that of the original axon. Amphid axons typically run ventrally from the cell body to the nerve ring (thick red line) and then proceed anterodorsally up the ring (see Fig. 5b, top). New axons can grow anterodorsally from the cell body to the nerve ring and then reverse to proceed down the ring posteroventrally (see Fig. 5b, middle). New axons can also sprout from a section of the dendrite close to the ring and follow the ring posteroventrally (see Fig. 5b, bottom). The functionality of the new axons is currently unknown; however, the latter regeneration scenario is unlikely to restore full functionality because the axon has sprouted off the dendrite. Axons can conduct electrical signals proximally and distally, while dendrites only conduct electrical signals proximally. Thus, the dendrite should be unable to supply its attached axon with outgoing electrical signals or participate in behaviors involving outgoing electrical signals.

Motor axons demonstrate the most regeneration capability and diversity; they even regenerate in the adult

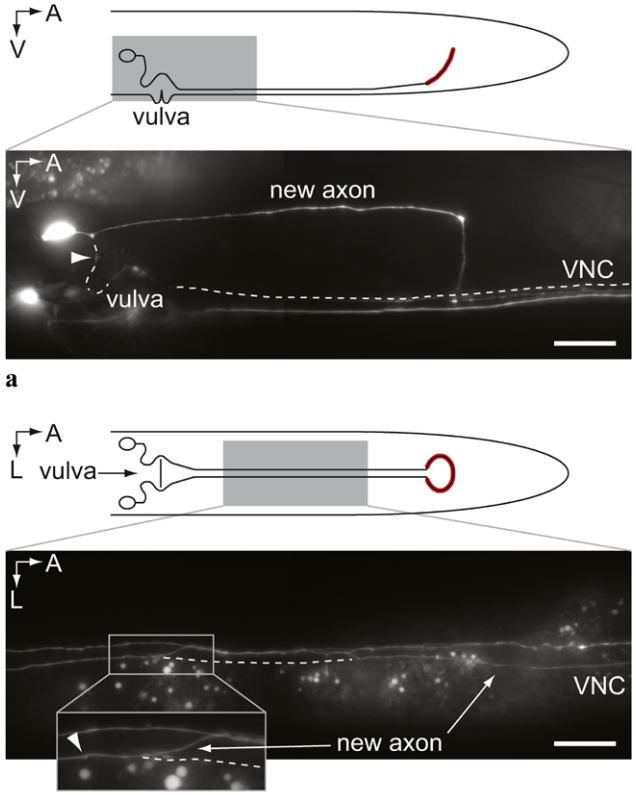

Fig. 6 HSN motor axon regenerates after surgery in young adult stage. Surgery locations marked by arrowheads. Decayed original axon marked with white dotted line in fluorescence images. Corner arrows show directions (ventral, left, anterior) in images. Scale bars are 20 µm. (**a**) Line drawing: lateral view of HSN neuron. Fluorescence image: after severing axon proximal to vulva, new axon extends anteriorly from cell body, turns ventrally, and then reaches the VNC. Image taken 42 h after surgery. (**b**) Line drawing: dorsal-ventral view of HSN neuron. Fluorescence image: after severing axon distal to vulva, new axon sprouts from severed tip (see *inset*) and travels along VNC. Image taken 19 h after surgery

stage [25, 26]. The HSN motor neuron, which controls egg laying, is an instructive example. The line drawings in Fig. 6 show lateral and dorsal-ventral views of the left and right HSNs. The neuron sends an axon ventrally to synapse with muscles that open the vulva for egg laying [27]. The axon continues anteriorly along the ventral nerve cord (VNC) to the nerve ring (thick red line) where it synapses to other neurons that increase the worm's locomotion velocity prior to egg laying [28]. Cutting the axon eliminates the neuron's contribution to different behaviors depending on the location of the cut. The location of the cut also determines whether the HSN regrows a new axon from the cell body or from the severed end. As shown in the fluorescence image in Fig. 6a, if the original axon is severed proximal to the vulva (surgery at arrowhead), the cell body extends a new axon which generally does not follow the path of the original axon (dotted line). In fact, some clearly nonfunctional axons improperly extend dorsally or posteriorly. If the original axon is severed distal to the vulva within the VNC, both the proximal section and the distal section can sprout new axons (see fluorescence image in Fig. 6b) but ablating the distal section into smaller segments prevents it from sprouting.

6 Summary

The submicrometer precision of femtosecond laser ablation in the bulk and the relatively simple and invariant neuronal circuit of *C. elegans* offer an opportunity to study the neuronal origins of behavior at a subcellular level. We developed a method for orienting worms so that the targets are more accessible for imaging and surgery. Pulses with energy above the energy threshold (about 1 nJ for 1.4 NA) result in complete dissection and keeping the energy near the threshold prevents collateral damage. Post-surgery reimaging is critical when cutting axons because they can regenerate. Finally, post-surgery assay reveals the contribution of the ablated neuronal part to generating behavior.

Acknowledgements Several people contributed to the work described in this paper. S.H.C. conceived of the basic idea for this work. S.H.C. also designed and carried out the experiments, and analyzed the results. S.H.C. acknowledges E.D. Diebold and G. Svacha for suggesting the vinyl record PDMS mold. Worm strains generously provided by J. Ahnn, S. Clark, P.G. Morgan, and P. Sengupta. Worm supplies generously provided by the laboratories of A.D.T. Samuel and Y. Zhang. E.M. supervised the research and the development of the manuscript. S.H.C. wrote the first draft of the manuscript; both authors subsequently took part in the revision process and approved the final copy of the manuscript. E.L. Chen, E.D. Diebold, T. Shih, and C. Evans provided feedback on the manuscript throughout its development. The research described in this paper was supported by the National Science Foundation under contracts DMR-0213805 and PHY-0555583.

References

1. S. Brenner, Genetics **77**, 71–94 (1974)
2. J.G. White, E. Southgate, J.N. Thomson, S. Brenner, Philos. Trans. B-Biol. Sci. **314**, 1–340 (1986)
3. J.E. Sulston, J.G. White, Dev. Biol. **78**, 577–597 (1980)
4. N. Shen, D. Datta, C.B. Schaffer, P. LeDuc, D.E. Ingber, E. Mazur, Mech. Chem. Biosyst. **2**, 17–25 (2005)
5. A. Vogel, V. Venugopalan, Chem. Rev. **103**, 577–644 (2003)
6. A. Vogel, J. Noack, G. Huttman, G. Paltauf, Appl. Phys. B **81**, 1015–1047 (2005)
7. C.L. Arnold, A. Heisterkamp, W. Ertmer, H. Lubatschowski, Opt. Express **15**, 10303–10317 (2007)
8. N. Bloembergen, IEEE J. Quantum Electron. **QE10**, 375–386 (1974)
9. R.R. Gattass, E. Mazur, Nat. Photon. **2**, 219–225 (2008)
10. C.B. Schaffer, A. Brodeur, E. Mazur, Meas. Sci. Technol. **12**, 1784–1794 (2001)
11. C.B. Schaffer, A. Brodeur, A.F. Garcia, E. Mazur, Opt. Lett. **26**, 93–95 (2001)
12. C.B. Schaffer, N. Nishimura, E.N. Glezer, A.M.T. Kim, E. Mazur, Opt. Express **10**, 196–203 (2002)

13. B.C. Stuart, M.D. Feit, A.M. Rubenchik, B.W. Shore, M.D. Perry, Phys. Rev. Lett. **74**, 2248–2251 (1995)
14. S.H. Chung, D.A. Clark, C.V. Gabel, E. Mazur, A.D. Samuel, BMC Neurosci. **7**, 30 (2006)
15. R.R. Gattass, L.R. Cerami, E. Mazur, Opt. Express **14**, 5279–5284 (2006)
16. M.H. Niemz, *Laser-Tissue Interactions: Fundamentals and Applications* (Springer, Berlin, 2004)
17. C.B. Schaffer, J.F. Garcia, E. Mazur, Appl. Phys. A **76**, 351–354 (2003)
18. E.N. Glezer, E. Mazur, Appl. Phys. Lett. **71**, 882–884 (1997)
19. M. Zhang, S.H. Chung, C. Fang-Yen, C. Craig, R.A. Kerr, H. Suzuki, A.D. Samuel, E. Mazur, R.W. Schafer, Curr. Biol. **18**, 1445–1455 (2008)
20. A. Heisterkamp, I.Z. Maxwell, E. Mazur, J.M. Underwood, J.A. Nickerson, S. Kumar, D.E. Ingber, Opt. Express **13**, 3690–3696 (2005)
21. R. Bar-Ziv, T. Tlusty, E. Moses, S.A. Safran, A. Bershadsky, Proc. Natl. Acad. Sci. USA **96**, 10140–10145 (1999)
22. Our unpublished observations
23. M.F. Yanik, H. Cinar, H.N. Cinar, A.D. Chisholm, Y. Jin, A. Ben-Yakar, Nature **432**, 822 (2004)
24. F. Bourgeois, A. Ben-Yakar, Opt. Express **15**, 8521–8531 (2007)
25. Z. Wu, A. Ghosh-Roy, M.F. Yanik, J.Z. Zhang, Y. Jin, A.D. Chisholm, Proc. Natl. Acad. Sci. USA **104**, 15132–15137 (2007)
26. C.V. Gabel, F. Antonie, C.F. Chuang, A.D. Samuel, C. Chang, Development **135**, 1129–1136 (2008)
27. C. Trent, N. Tsung, H.R. Horvitz, Genetics **104**, 619–647 (1983)
28. L.A. Hardaker, E. Singer, R. Kerr, G. Zhou, W.R. Schafer, J. Neurobiol. **49**, 303–313 (2001)